Yang et al. EJNMMI Physics (2024) 11:70
https://doi.org/10.1186/s40658-024-00673-9

EJNMMI Physics

ORIGINAL RESEARCH Open Access

Automatic reorientation to generate short-axis myocardial PET images

Yuling Yang[1,2], Fanghu Wang[3], Xu Han[1,2], Hui Xu[4], Yangmei Zhang[1,2], Weiping Xu[3], Shuxia Wang[3] and Lijun Lu[1,2,5*]

*Correspondence:
Lijun Lu
ljlubme@gmail.com
[1]School of Biomedical Engineering, Southern Medical University, 1023 Shatai Road, Guangzhou 510515, China
[2]Guangdong Provincial Key Laboratory of Medical Image Processing, Southern Medical University, 1023 Shatai Road, Guangzhou 510515, China
[3]PET Center, Department of Nuclear Medicine, Guangdong Provincial People's Hospital, Guangdong Academy of Medical Sciences, Southern Medical University, 106 Zhongshan Er Road, Guangzhou 510080, China
[4]The Cancer Hospital of the University of Chinese Academy of Sciences (Zhejiang Cancer Hospital), Hangzhou, Zhejiang, China
[5]Pazhou Lab, Guangzhou 510515, China

Abstract

Background Accurately redirecting reconstructed Positron emission tomography (PET) images into short-axis (SA) images shows great significance for subsequent clinical diagnosis. We developed a system for automatic redirection and quantitative analysis of myocardial PET images.

Methods A total of 128 patients were enrolled for 18 F-FDG PET/CT myocardial metabolic images (MMIs), including 3 image classifications: without defects, with defects, and excess uptake. The automatic reorientation system includes five modules: regional division, myocardial segmentation, ellipsoid fitting, image rotation and quantitative analysis. First, the left ventricular geometry-based canny edge detection (LVG-CED) was developed and compared with the other 5 common region segmentation algorithms, the optimized partitioning was determined based on partition success rate. Then, 9 myocardial segmentation methods and 4 ellipsoid fitting methods were combined to derive 36 cross combinations for diagnostic performance in terms of Pearson correlation coefficient (PCC), Kendall correlation coefficient (KCC), Spearman correlation coefficient (SCC), and determination coefficient. Finally, the deflection angles were computed by ellipsoid fitting and the SA images were derived by affine transformation. Furthermore, the polar maps were used for quantitative analysis of SA images, and the redirection effects of 3 different image classifications were analyzed using correlation coefficients.

Results On the dataset, LVG-CED outperformed other methods in the regional division module with a 100% success rate. In 36 cross combinations, PSO-FCM and LLS-SVD performed the best in terms of correlation coefficient. The linear results indicate that our algorithm (LVG-CED, PSO-FCM, and LLS-SVD) has good consistency with the reference manual method. In quantitative analysis, the similarities between our method and the reference manual method were higher than 96% at 17 segments. Moreover, our method demonstrated excellent performance in all 3 image classifications.

Conclusion Our algorithm system could realize accurate automatic reorientation and quantitative analysis of PET MMIs, which is also effective for images suffering from interference.

Keywords Positron emission tomography (PET), Automatic reorientation, Regional division, Image segmentation, Fitting algorithm

Introduction

Positron emission tomography (PET) is increasingly being used routinely in the diagnosis of coronary artery disease [1, 2]. Compared to single-photon emission computed tomography (SPECT), PET has high resolution images and quantitative parameters in myocardial images [3, 4]. The myocardial PET image is a longitudinal image perpendicular to the patient's long axis but not perpendicular to the left ventricular long axis. However, the direction of the long axis of the left ventricle is inconsistent with that of the human body [5]. The left ventricle is located below the left back of the right atrium, and the direction of its long axis slopes from the upper right to the lower left of the body with individual differences [6, 7]. Moreover, other organs and tissues around the heart also affected the observation field. Tracer uptakes were also observed in the right atrium, coronary sinus, and spine, which appeared as bright areas in the image [8, 9].

In order to facilitate clinical diagnosis and accurate quantitative analysis, the longitudinal image needs to be reoriented and rotated to obtain a cardiac short-axis (SA) image perpendicular to the left ventricular long axis [10]. Currently, steering studies focused on cardiac PET images are scarce, and most physicians adopted the traditional method manual for reorientation in clinical applications. SPECT as the mainstream imaging for cardiac disease, the related reorientation algorithms can be divided into traditional and automatic modes [11–17].

Traditional manual positioning mainly relies on the operator's personal experience. According to visual judgment, the operator draws the long axis of the myocardium on horizontal long-axis (HLA) images and vertical long-axis (VLA) images to obtain the deviation angle, and then rotates the images to obtain SA images. However, this process is time-consuming, poorly repeatable, and error-prone [16].

The automatic algorithm obtains SA SPECT images through myocardial segmentation and model fitting. Employing techniques such as maximum radiation labeling or iterative clustering, the left ventricular myocardium could be segmented from SPECT images [11–13]. Subsequently, the left ventricular myocardium is fitted to an approximate model through model fitting, this step can calculate the left ventricular deviation angle, which is used to rotate the cardiac SPECT image and generate the SA SPECT image [14, 15].

Severe defects may lead to inaccurate positioning of the left ventricular long axis, so in clinical software such as Auto QUANT and Emory Cardiac Toolbox, the operator can manually adjust the long axis vector to ensure accurate reorientation [16–20]. Recently, the latest development of deep learning has also successfully introduced reorientations. For instance, Zhang et al. adopted convolutional neural networks (CNN) to predict six rigid body transformation parameters and obtained SA SPECT images by spatial transformation network [21].

However, the image quality of PET images is higher than that of SPECT images [22]. PET images can not only provide more detailed information about the left ventricle but also provide information about surrounding organs and tissues, which can serve as interference information and affect the accuracy of automatic reorientation [23–25]. Thus, the methods of SPECT may not be suitable for PET images.

Recent works related to myocardial PET images mostly focused on myocardial perfusion images (MPIs) and myocardial metabolic images (MMIs). In this work, MMI data was collected analyzed since it is widely used in China. The report of Su et al. has shown that segmenting the image into regions and extracting the heart part separately could improve the efficiency of subsequent segmentation [26]. Given that, we added the step of region division before traditional myocardial segmentation and model fitting.

In total, the purpose of our research is to find a set of automatic reorientation algorithms that are most suitable for 18 F-FDG PET MMIs. 6 methods of region division were adopted and compared, and the performances of 36 cross-combinations derived from 9 myocardial segmentation methods and 4 model fitting methods were evaluated.

Methods and materials

Study population

This study initially included 135 patients who underwent the 18 F-FDG PET/CT scanning on a Siemens Biography 16 PET/CT scanner at the Guangdong Provincial People's Hospital from 2017 to 2019. However, 7 patients were excluded due to the following reasons: (1) poor image quality, or (2) incomplete clinical information. Finally, 128 PET/CT MMIs were included in the experiment, among them, 108 were coronary artery disease (CAD) patients, and the remaining 20 patients included heart failure, heart valvular disease, coronary artery aneurysm, and other cardiovascular diseases. Patient characteristics of 128 18 F-FDG PET MMIs are listed in Table 1. The study was approved by the institutional review board.

Two nuclear medicine doctors with 3 years of clinical experience utilized PMOD software to confirm the SA images corresponding to the PET MMIs data. The disputed cases were individually reviewed and reconfirmed by a nuclear medicine doctor with 13 years of clinical experience to obtain the reference reorientation images and reference reorientation angles for each case. The reference reorientation images were quantitatively analyzed by polar maps and the summed metabolism score (SMS). Cases with SMS>2 were classified as patients with myocardial metabolic defect, and the cases with SMS<=2 were divided into patients without myocardial metabolic defect and patients with right ventricle excess uptake after visual examination by two nuclear medicine doctors. The dataset was specifically divided into 48 patients without myocardial metabolic

Table 1 Patient characteristics of 128 PET MMIs

Characteristic	*N* = 128
Age (years)	56.9 (5–81)
Gender	
Male	89.8% (115 / 128)
Female	10.2% (13 / 128)
Weight (kg)	63.5 (19.5–93)
Heart rate (times/minute)	75 (48–117)
Systolic blood pressure (mmHg)	115 (81–172)
Diastolic blood pressure (mmHg)	74 (47–109)
Hypertension	53 (41.4%)
Diabetes	35 (27.3%)
Smoking	43 (33.6%)
With CAD	108 (84.4%)
Without CAD	20 (15.6%)
MMIs without defects	48
MMIs with defects	49
MMIs with right ventricle excess uptake	31

CAD: Coronary artery disease;

MMI: Myocardial metabolism image

defect, 49 patients with myocardial metabolic defect, and 31 patients with right ventricle excess uptake.

Before the MMI scan, each patient underwent a glucose loading test. The patient's blood glucose was measured after 45 min of the glucose loading test, and the insulin dosage by injecting insulin based on the patient's blood glucose level. Check the patient's blood sugar level every half hour, the 18 F-FDG was intravenously injected at a standard dose of 0.1mCi/Kg once the patient's blood glucose level was at or below 7.8mmol/L. After a resting period of 90 min, each patient underwent a PET/CT scan. The scanning process was conducted sequentially, starting with a CT localization scan (120kVp, 10 mA), followed by a CT tomography scan (140kVp, 80 mA), and finally a 15-minute list mode PET scan. MMI images were reconstructed using attenuation-weighted ordered subset expectation maximization (two iterations, 24 subsets) and a Gaussian filter (FWHM = 5 mm). CT-based attenuation, scatter, decay, and random corrections were applied to the reconstructed images.

The proposed cardiac PET image automatic reorientation system consisted of five modules. As shown in Fig. 1, there are regional division, myocardial segmentation, ellipsoid fitting, image rotation and quantitative analysis. The inputs were 18 F-FDG PET MMIs, and the outputs were SA images and the quantitative analysis results.

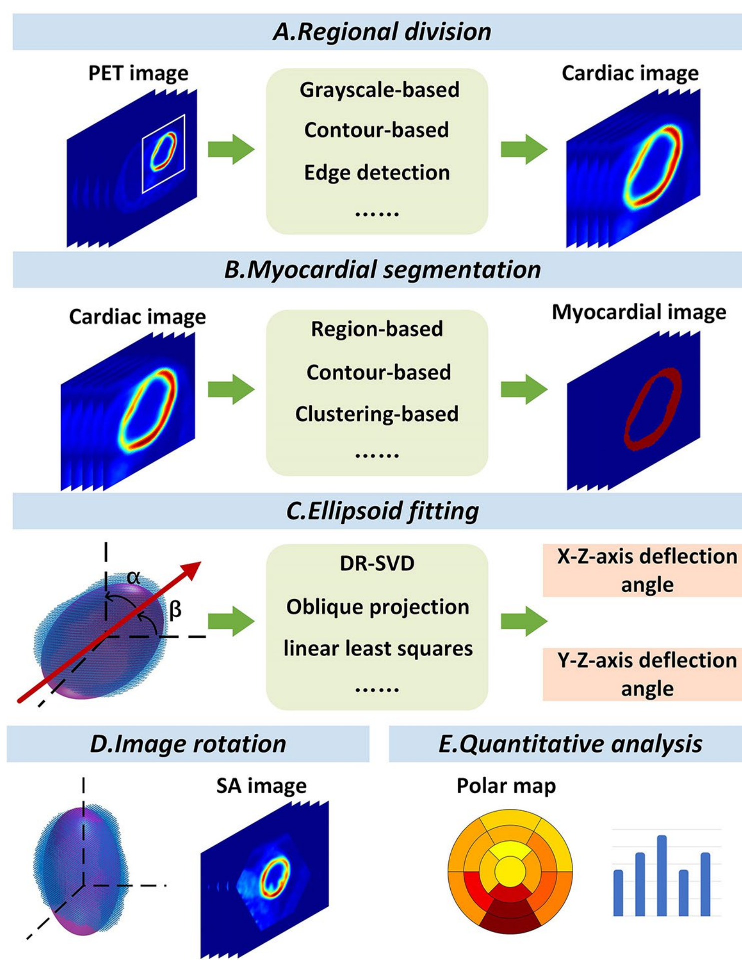

Fig. 1 Overview of the cardiac PET image automatic redirection system, including regional division, myocardial segmentation, ellipsoid fitting, image rotation, and quantitative analysis

Regional division

The region-based division method is an image division technique that divides an image into several regions. Dividing the area containing the left ventricle in 18 F-FDG PET MMIs can remove the interference from other organs and tissues, which is beneficial for subsequent myocardial segmentation [26]. The myocardial PET images after regional division are resampled to a unified size of 80 * 80 * 64. One of the most common algorithms for region division is edge detection. We proposed the LVG-CED method, which improved the canny edge detection algorithm by introducing left ventricular position and size information as prior conditions. This method removed the areas that do not satisfy the conditions to improve partition efficiency and adopted the active contour algorithm with excellent performance in medical image division. Also, we compared some popular traditional algorithms for region partitioning of 18 F-FDG PET MMIs, including watershed [27], reconstruction closure (RC), iterative threshold segmentation (ITS) [28, 29], local fitting-based active contour models (LF-ACM) [30, 31], curve evolution (CE) [32], and LVG-CED.

Myocardial segmentation

Through segmentation algorithms, we can segment the left ventricular myocardium from myocardial PET images. Segmentation algorithms are mainly divided into three categories: region-based methods, contour-based methods, and clustering-based methods [33, 34]. Region-based methods such as region partitioning and region growth are suitable for segmenting small regions. For the contour method, we selected an active contour driven by region scalable fitting and introduced a Gaussian energy Laplace operator optimization algorithm. Clustering-based algorithms are the most common and widely used segmentation methods. We compared the clustering performance of k-means and fuzzy C-means and used a particle swarm optimization algorithm to improve the speed and accuracy of clustering. In this study, a total of 9 segmentation algorithms were adopted for comparison, including maximum radioactivity sampling (MRS) [15], splitting and merging (SM) [35], region growth (RG) [34], multiplicative intrinsic component optimization (MICO) [36, 37], active contours driven by region-scalable fitting and optimized Laplacian of Gaussian energy (RSF-LOG) [38, 39], K-means, fuzzy C-means (FCM), particle swarm optimization K-means (PSO-K-means) [40], and particle swarm optimization fuzzy C-means (PSO-FCM) [41]. All the mentioned methods are fully automatic unsupervised segmentation algorithms that eliminate the need for manual adjustment or labeled data.

Ellipsoid fitting

The shape of the human left ventricular myocardium is irregular, thus it is usually fitted by a hemisphere of a cylinder with a hemisphere, a cone, or an ellipsoid [11, 42, 43]. We chose to fit it as an ellipsoid, and the formula is shown in Eq. (1).

$$a_1x^2 + a_2y^2 + a_3z^2 + a_4xy + a_5xz + a_6yz + a_7x + a_8y + a_9z + a_{10} = 0 \tag{1}$$

Where $\mathrm{a_i}$, i = 1, 2, …10 are the 10 parameters of the ellipsoid. Based on the ellipsoid parameters, the long-axis deflection angle of the ellipsoid could be approximated as the left ventricular deflection angle, as shown in Eq. (2) and Eq. (3).

$$\alpha = \frac{1}{2}\tan^{-1}\frac{\sqrt{2}a_6}{a_2 - a_3} \tag{2}$$

$$\beta = \frac{1}{2}\tan^{-1}\frac{\sqrt{2}a_4}{a_2 - a_1} \tag{3}$$

Where α is the X-Z axis deviation angle, and β is the Y-Z axis deviation angle. The fitting algorithm of Douglas Rachford singular value decomposition (DR-SVD) [44], oblique projection (OP), linear least squares (LLS), and linear least squares singular value decomposition (LLS-SVD) were used separately.

Image rotation

According to two deflection angles, we calculated the corresponding rotation matrices, and used affine transformation to rotate 18 F-FDG PET MMIs. The formulas as shown in Eqs. 4 and 5.

$$H_1 = \begin{bmatrix} 1 & 0 & 0 \\ 0 & \cos\alpha & -\sin\alpha \\ 0 & \sin\alpha & \cos\alpha \end{bmatrix} \tag{4}$$

$$H_2 = \begin{bmatrix} \cos\beta & 0 & \sin\beta \\ 0 & 1 & 0 \\ -\sin\beta & 0 & \cos\beta \end{bmatrix} \tag{5}$$

where α is the X-Z axis deviation angle, and β is the Y-Z axis deviation angle. We cropped and resampled the rotated images to obtain SA images of the same size as 18 F-FDG PET MMIs.

Quantitative analysis

Polar maps were used to quantitatively analyze the results of automatic orientation. Relied on the hemisphere plus cylinder model proposed by Carci et al. [42], the left ventricle apex was fitted by a hemisphere, the base and the mid-cavity was fitted by a cylinder. Referring to the criterions proposed by the American Heart Association [45], the polar map was divided into 17 segments and 3 blood supply vessel regions. The left anterior descending (LAD) consisted of 7 segments: 1, 2, 7, 8, 13, 14, 17. The right coronary artery (RCA) consisted of 5 segments: 3, 4, 9, 10, 15. The left circumflex (LCX) consisted of 5 segments: 5, 6, 11, 12, 16. The images manually positioned and rotated by clinical physicians were used as reference images. The similarity between the results obtained by our method and those obtained from reference images was calculated by Eq. (6).

$$\mathrm{m} = \left|1 - \frac{p_r - p_o}{p_o}\right| \times 100\% \tag{6}$$

where p_r is the value of the polar map corresponding to the reference image, p_0 is the value of the polar map corresponding to the image obtained from our method, and m is the similarity. We analyzed the results of 17 segments, 3 blood supply vessel regions, and the overall polar map in detail.

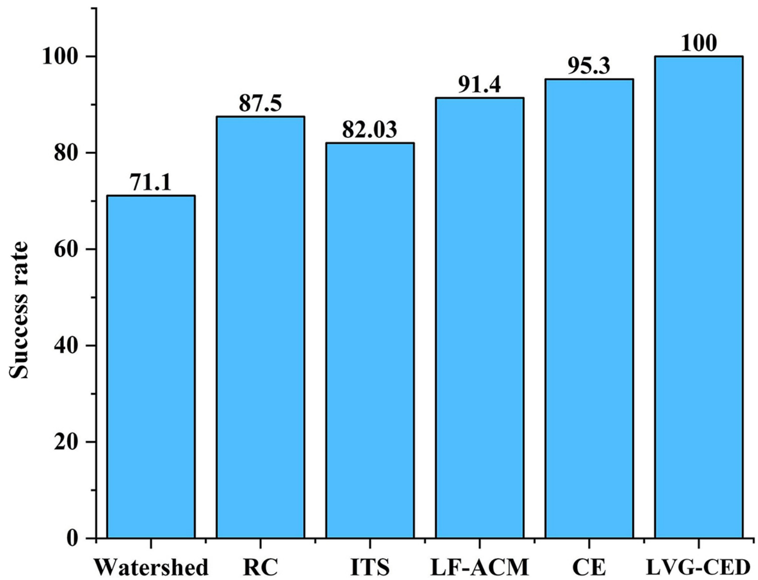

Fig. 2 Statistical results of successfully dividing cardiac regions of 128 PET MMIs. RC: reconstruction closure, ITS: iterative threshold segmentation, LF-ACM: local fitting-based active contour models, CE: curve evolution, LVG-CED: left ventricular geometry-based canny edge detection

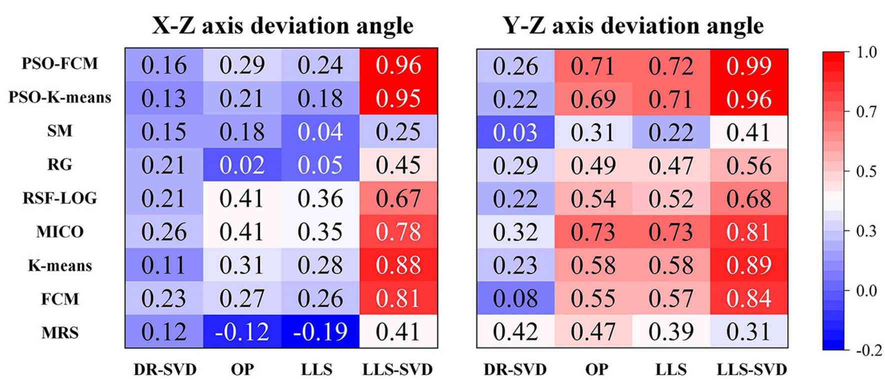

Fig. 3 Heat map depicting the Pearson correlation coefficients of paired myocardial segmentation and ellipsoid fitting methods. MRS: maximum radioactivity sampling, SM: splitting and merging, RG region growth, MICO: multiplicative intrinsic component optimization, RSF-LOG: active contours driven by region-scalable fitting and optimized Laplacian of Gaussian energy, FCM: fuzzy C-means, PSO-K-means: particle swarm optimization K-means, PSO-FCM: particle swarm optimization fuzzy C-means, DR-SVD: Douglas Rachford singular value decomposition, OP: oblique projection, LLS: linear least squares, LLS-SVD: linear least squares singular value decomposition

Results

Parameter-level analysis

Figure 2 shows the statistical results of the regional division. The method was evaluated based on whether the entire heart region was completely divided. The success rate of LVG-CED was as high as 100%, and the success rate of CE was 95.3%.

The algorithm for the regional division was fixed as LVG-CED. We cross combined 9 myocardial segmentation methods and 4 ellipsoid fitting methods and compared the results with the manual method. The paired Pearson correlation coefficient (PCC) of different myocardial segmentation methods (in columns) and ellipsoid fitting methods (in rows) are shown in Fig. 3. Among them, the combination of PSO-FCM and LLS-SVD showed the highest performance (X-Z PCC: 0.96; Y-Z PCC: 0.99), followed by the

Table 2 The Pearson correlation coefficients of cross-combined myocardial segmentation methods and ellipsoid fitting methods

Pearson	X-Z axis deviation angle				Y-Z axis deviation angle			
	DR-SVD	OP	LLS	LLS-SVD	DR-SVD	OP	LLS	LLS-SVD
MRS	0.12	-0.12	-0.20	0.40	0.42	0.47	0.39	0.31
SM	0.23	0.27	0.26	0.81	0.08	0.55	0.57	0.84
RG	0.11	0.31	0.28	0.88	0.23	0.58	0.58	0.89
MICO	0.26	0.41	0.35	0.78	0.32	0.73	0.73	0.80
RSF-LOG	0.21	0.40	0.36	0.67	0.20	0.54	0.52	0.68
K-means	0.21	0.02	0.05	0.45	0.29	0.49	0.47	0.56
FCM	0.15	0.18	0.04	0.25	0.03	0.30	0.22	0.40
PSO-K-means	0.13	0.20	0.18	0.95	0.22	0.71	0.70	0.96
PSO-FCM	0.16	0.29	0.24	**0.96**	0.26	0.70	0.70	**0.99**

MRS: Maximum radioactivity sampling, SM: Splitting and merging, RG: Region growth, MICO: Multiplicative intrinsic component optimization, RSF-LOG: Active contours driven by region-scalable fitting and optimized Laplacian of Gaussian energy, FCM: Fuzzy C-means, PSO-K-means: Particle swarm optimization K-means, PSO-FCM: Particle swarm optimization fuzzy C-means

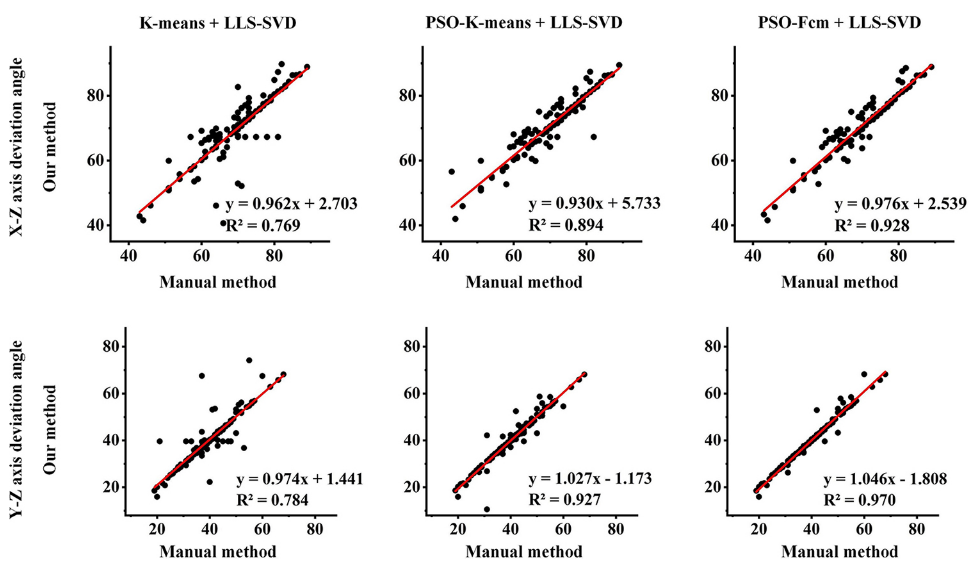

Fig. 4 The linear regression plots between the predicted angles from our method and the reference angles from the manual method contain three best-performing combinations, in order: K-means + LLS-SVD, PSO-K-means + LLS-SVD, and PSO-FCM + LLS-SVD. The first row is the linear fitting results on the X-Z axis deflection angle, and the second row is the linear fitting results on the Y-Z axis deflection angle

combination of PSO-K-means and LLS-SVD (X-Z PCC: 0.95; Y-Z PCC: 0.96). The relevant results obtained by comparing cross combinations and the manual method are presented in Table 2, Supplementary Tables 1 and 2, which are PCC, Kendall correlation coefficient (KCC), and Spearman correlation coefficient (SCC), respectively. The results of similarity coefficient showed that the combination of PSO-FCM and LLS-SVD had an excellent agreement with the manual method (X-Z KCC: 0.87; Y-Z KCC: 0.95; X-Z SCC: 0.96; Y-Z SCC: 0.99).

To assess the accuracy and reliability of different combined traditional algorithms, Fig. 4 shows the linear fitting effects between the two deflection angles and the true value. The first column shows the linear regression coefficients of the predicted angle and the manual method on the X-Z deflection angle, and the second column shows the coefficients on the Y-Z deflection angle. The combinations from left to right were:

Table 3 The correlation coefficient between existing methods and our method

	X-Z axis deviation angle			Y-Z axis deviation angle		
	Kendall	**Pearson**	**Spearman**	**Kendall**	**Pearson**	**Spearman**
TG	0.34	0.39	0.47	0.38	0.40	0.51
MRS	0.24	0.40	0.34	0.25	0.31	0.33
Our Method	**0.87**	**0.96**	**0.96**	**0.95**	**0.99**	**0.99**

TG: Topological goniometry

MRS: Maximum radioactivity sampling

Table 4 The similarities of the 17 segments and the 3 blood supply vessel regions among 128 patients

Segment	**1**	**2**	**3**	**4**	**5**
Similarity (%)	96.74 ± 7.20	98.01 ± 5.25	98.64 ± 3.58	97.16 ± 10.19	96.89 ± 10.91
Segment	6	7	8	9	10
Similarity (%)	97.72 ± 4.61	97.47 ± 7.08	97.95 ± 6.26	**98.89 ± 3.82**	97.75 ± 4.89
Segment	11	12	13	14	15
Similarity (%)	97.59 ± 7.31	98.50 ± 3.13	96.84 ± 17.29	98.55 ± 5.96	98.47 ± 6.49
Segment	16	17			
Similarity (%)	97.82 ± 9.46	98.27 ± 5.13			
blood supply vessel region	LAD	RCA		LCX	
Similarity (%)	97.69 ± 6.16	**98.18 ± 4.54**		97.70 ± 5.51	
Total Similarity (%)	**97.84 ± 4.86**				

LAD: left anterior descending

RCA: right coronary artery

LCX: left circumflex

K-means + LLS-SVD, PSO-K-means + LLS-SVD, and PSO-FCM + LLS-SVD. It is observed that the combination of PSO-FCM and LLS-SVD showed the best consistent results, with determination coefficients of 0.928 and 0.970, respectively.

Moreover, we compared our method with existing methods: topological goniometry (TG) [15] and MRS, the results of the correlation coefficients between the two reorientation angles are shown in Table 3. Our method performed best on all three correlation coefficients, while KCCs were 0.87 and 0.95, PCCs were 0.96 and 0.99, and SCCs were 0.96 and 0.99, respectively.

Clinical quantitative analysis

To further verify the reliability of our method, Table 4 shows the similarity between the selected optimal combination (LVG-CED, PSO-FCM, and LLS-SVD) and the manual method for quantitative analysis of the poplar map. Similarities of all 17 segments were more than 96%, the similarity of the mid inferoseptal had the highest similarity (98.89%) among 17 segments, RCA had the highest similarity (98.18%) among 3 blood supply vessel regions, and the overall average similarity of the left ventricle was 97.84%.

Figure 5 shows the linear regression result of 17 segments of 128 patients' polar maps (2142 segments in total). The optimal combination (LVG-CED, PSO-FCM, and LLS-SVD) was highly consistent with the manual method, and the determination coefficient was as high as 0.992.

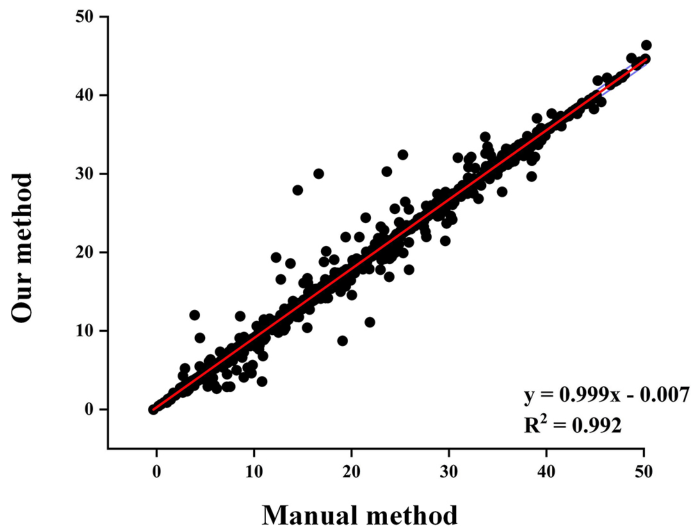

Fig. 5 The linear regression plot between the 2176 segment values calculated using our method and the reference segment values using the manual method

Image-level analysis

Figure 6 shows the PET images of four patients, including reconstructed images, reference images, images obtained by our method (LVG-CED, PSO-FCM, and LLS-SVD), and corresponding polar maps of SA images.

Patient #49,365 without defects, mild ischemia of the basal anterolateral didn't affect the automatic reorientation, and the images obtained by our method were highly consistent with reference images. Patient #49,641 and patient #42,151 are two cases with interferences. The green shear in Fig. 6 pointed out an apical ischemia, and the yellow shear in Fig. 6 pointed out an excessive uptake of the right ventricle. Both cases had interferences with the automatic reorientation, but our method still exhibited good performance. However, when the concentration of excess uptakes and left ventricular uptakes was similar (patient #48,223), it might still affect the effectiveness of the automatic redirection and cause inaccuracies in subsequent quantitative analysis.

Specific classification analysis

Table 5 shows the correlation analysis results obtained by comparing our method and the manual method under three different image classifications. It included MMIs without defects, MMIs with defects, and MMIs with right ventricle excess uptake. our method achieved high consistency with the manual method in all three types of patients. The similarity of MMIs without defects was the highest, and the similarity of MMIs with right ventricle excess uptake was the lowest, while KCCs were 0.736 and 0.891, PCCs were 0.948 and 0.968, and SCCs were 0.879 and 0.964, respectively.

Discussion

In this study, we developed an algorithm system for automatic left ventricular reorientation and simultaneous quantitative analysis on 18 F-FDG PET MMIs. Our algorithm system included five parts: regional division, myocardial segmentation, ellipsoid fitting, image rotation, and quantitative analysis. We compared 6 regional segmentation methods and 36 cross combinations (9 myocardial segmentation methods and 4 ellipsoid

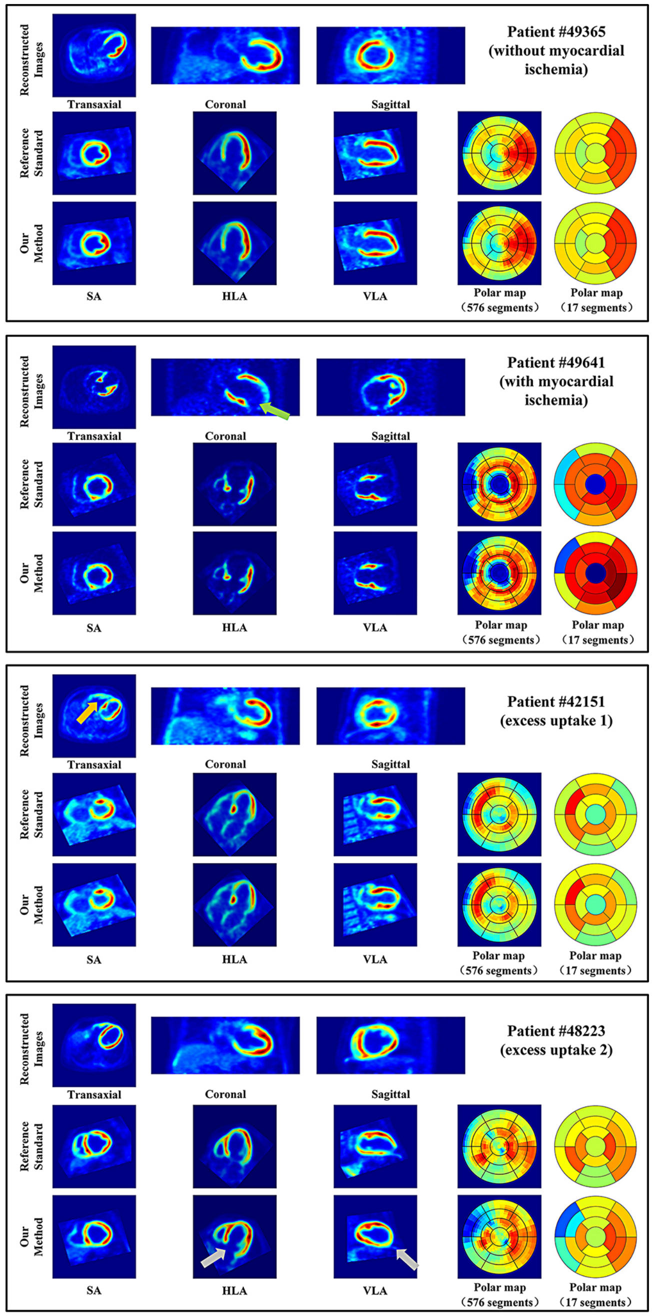

Fig. 6 Reconstructed images, reference reoriented images by the manual method, and reoriented images by our method for four PET MMIs: patient #49,365 without defects, patient #49,641 with defects, while patient #42,151 and patient #48,223 have excess uptake. For each, (i) reconstructed images are shown (From left to right): Transaxial, coronal, and sagittal 3 orthogonal orientations, (ii) reference reoriented images by the manual method and (iii) reoriented images by our method are shown (From left to right): SA, HLA, VLA, polar map (576 segments) and polar map (17 segments). SA: short axis, HLA: horizontal long axis, VLA: vertical long axis

fitting methods) and ultimately chose the best performing method as our method: LVG-CED, PSO-FCM, and LLS-SVD. Compared to the manual method, our method showed a high consistency at both the image level and the quantitative analysis level.

In the regional division module, we chose LVG-CED in our system. The prior knowledge of heart contour can improve the accuracy of detection [46]. In our study, the prior knowledge provided the information of left ventricular location and size, and edge

Table 5 The 3 correlation coefficients under 3 types of image classification

	X-Z axis deviation angle			Y-Z axis deviation angle		
	Kendall	Pearson	Spearman	Kendall	Pearson	Spearman
MMIs without defects	**0.919**	**0.984**	**0.980**	**0.986**	**0.999**	**0.998**
MMIs with defects	0.859	0.959	0.959	0.932	0.976	0.982
MMIs with right ventricle excess uptake	0.736	0.948	0.879	0.891	0.968	0.964

MMI: Myocardial metabolic image

detection effectively detected the left ventricular myocardial edge. The success rate of partitioning the left ventricular region on our dataset was 100%, which was higher than all other traditional partitioning algorithms (Fig. 2).

In previous studies, various algorithms such as maximum radiation sampling, clustering, feature extraction, threshold partitioning, etc. have been used for myocardial segmentation [10–20]. However, due to different datasets, different preprocessing methods, and other variables, it is not possible to integrate and compare these methods. In our study, we used a total of 9 popular traditional segmentation algorithms for myocardial segmentation. In terms of model fitting selection, a cylinder with a hemisphere, a cone, or a ellipsoid have been used to fit the model of left ventricular myocardium, but the fitting effect of the first two models was poor in the areas with severe ischemia, which affects the accuracy of subsequent reorientation [11, 42]. The ellipsoid was similar in shape to the left ventricle and less affected by defects [43], and it was selected as the myocardium fitting model. The combination of myocardial segmentation and ellipsoid fitting had the best similarity coefficient among PSO-FCM and LLS-SVD. On the X-Z axis deviation angle, KCC, PCC and SCC were 0.87, 0.96 and 0.96 respectively, and were 0.95, 0.99 and 0.99 on the Y-Z axis deviation angle as shown in Table 2, Supplementary Tables 1 and 2.

At present, software for fully automatic PET cardiac image reorientation has not been applied in clinical diagnosis. Through semi-automatic methods, doctors manually adjust the results of the software's automatic segmentation of fixed points to determine rotation parameters and obtain SA images, it has low repeatability and large errors [16]. However, due to the difficulty in obtaining PET data, there are rare studies focused on automatic reorientation of 18 F-FDG PET MMIs, and existing studies mainly focus on SPECT images. For instance, Zhang et al. used 322 SPECT images, and the determination coefficients of three rotation parameters were 0.928, 0.958, and 0.994 respectively [21]. Zhu et al. used 254 SPECT images, and the determination coefficients of three rotation parameters were 0.987, 0.990, and 0.996 respectively [22]. On our data set of 128 cases of 18 F-FDG PET MMIs, our method achieved similar results with the determination coefficients of 0.928 and 0.970 (Fig. 4).

The polar map, as the best semi quantitative method for visual interpretation of regional left ventricular abnormalities, was selected as the clinical quantitative analysis method in our study [47]. The linear fitting results of Fig. 5 indicated that the polar map values obtained through our method were highly consistent with the results obtained through the manual method (determination coefficient: 0.9915). The similarities were higher than 96% in all 17 segments, with the mid inferoseptal segment having the highest similarity (98.89%). Besides, we found that the similarity of RCA was the highest among the 3 blood supply vessel regions, at 98.18%, the total similarity of the polar maps corresponding to 128 18 F-FDG PET MMIs was 97.84% (Table 4).

In the study of automatic reorientation of the left ventricle, there are two main difficulties: (1) Defects, which may lead to insufficient myocardial imaging on PET images, increasing the difficulty of model fitting and introducing errors in ellipsoid fitting [11, 15]; (2) Excess uptakes, when additional tracer uptake is present in the organs and tissues surrounding the left ventricle, may be mistaken for the left ventricle, introducing errors in myocardial segmentation. Either of these situations can result in the failure of automatic redirection [16–18]. Based on these two difficulties, we divide images into three categories: MMIs without defects, MMIs with defects and MMIs with right ventricle excess uptake. As shown in Fig. 6, our method performed well under all 3 classifications, and the SA images and polar maps obtained by our method had good agreement with those obtained by the manual method. Also notice that MMIs with defects showed higher correlation coefficients than that from MMIs with right vehicle excess uptake (KCC: 0.859 and 0.932 vs. 0.736 and 0.891, PCC: 0.959 and 0.976 vs. 0.948 and 0.968, SCC: 0.959 and 0.982 vs. 0.879 and 0.964). The errors caused by defects can be reduced to some extent by ellipsoid fitting, but the excess uptake is not easy to distinguish from the left ventricular myocardium, and the impact of the results is greater.

Our study had several limitations. First, as shown in Fig. 6, when the distances between the right ventricle and the left ventricle were close and the uptake intensities were similar, myocardial segmentation errors may occur, leading to errors in subsequent automatic reorientation. However, due to the close distance, the angle errors were still less than 20 degrees. Second, the methods we used are all traditional algorithms. In recent years, deep learning has shown excellent performance in medical image processing. In subsequent experiments, we hope to collect more PET data and introduce deep learning into automatic reorientation to further compare and organize with traditional algorithms.

Conclusion

We developed an algorithm system for automatic reorientation and quantitative analysis of 18 F-FDG PET MMIs. Our results showed that the system was highly consistent with the manual method at both the image level and the quantitative analysis level. Further, it achieved good performance on three different image classifications (MMIs without defects, MMIs with defects, and MMIs with right ventricle excess uptake).

Abbreviations

PET	Positron emission tomography
SPECT	Single-photon emission computed tomography
SA	Short-axis
HLA	Horizontal long-axis
VLA	Vertical long-axis
MMI	Myocardial metabolic image
MPI	Myocardial perfusion images
CAD	Coronary artery disease
SMS	Summed metabolism score
PCC	Pearson correlation coefficient
KCC	Kendall correlation coefficient
SCC	Spearman correlation coefficient

Supplementary Information

The online version contains supplementary material available at https://doi.org/10.1186/s40658-024-00673-9.

Supplementary Material 1

Acknowledgements
The authors extend gratitude to the staff at Guangdong Provincial People's Hospital (Guangdong Academy of Medical Sciences) for their invaluable support in clinical endeavors.

Author contributions
XH, HX, YZ, LL and YY contributed to the design of the research. Material preparation and data collection were conducted by FW, WX and SW. YY performed data analysis and modeling. The initial draft of the manuscript was written by YY, with all authors contributing to the drafting and revisions of the manuscript. All authors read and approved the final manuscript.

Funding
This study was funded by the National Natural Science Foundation of China (62371221, 12326616, 62201245 and 32101108), National High-end Foreign Experts Recruitment Plan (G2023030025L), Guangdong Basic and Applied Basic Research Foundation (2020A1515110683 and 2021A1515011676) and the Science and Technology Program of Guangdong Province 2022A0505050039.

Data availability
The datasets utilized or analyzed in the present study are accessible from the corresponding author upon a reasonable request.

Declarations

Ethics approval and consent to participate
Not applicable.

Consent for publication
Not applicable.

Competing interests
Not applicable.

Received: 14 November 2023 / Accepted: 19 July 2024
Published online: 02 August 2024

References

1. Carli MFD, Dorbala S, Meserve J, Fakhri GE, Sitek A, Moore SC. Clinical myocardial perfusion PET/CT. Journal of nuclear medicine: official publication. Soc Nuclear Med 2007,48(5).
2. Schindler TH, Schelbert HR, Quercioli A, Dilsizian V. Cardiac PET imaging for the detection and monitoring of coronary artery Disease and Microvascular Health. JACC: Cardiovasc Imaging 2010,3(6).
3. George A, Gregory G, Georgios K et al. SPECT and PET in ischemic heart failure. Heart Fail Rev 2017,22(2).
4. Bateman TM. Advantages and disadvantages of PET and SPECT in a busy clinical practice. J Nuclear Cardiology: Official Publication Am Soc Nuclear Cardiol 2012,19 Suppl 1(Suppl.1).
5. Greenbaum RA, Ho SY, Gibson DG, Becker AE, Anderson RH. Left ventricular fibre architecture in man. Br Heart J 1981,45(3).
6. King LS. An anatomical disputation concerning the Movement of the heart and blood in living creatures. JAMA: J Am Med Association 1977,238(7).
7. Henein MY, Gibson DG. Normal long axis function. Heart 1999,81(2).
8. Namdar M, Hany TF, Koepfli P, Siegrist PT, Burger C, Wyss CA et al. Integrated PET/CT for the assessment of coronary artery disease: a feasibility study. J Nuclear Medicine: Official Publication, Society of Nuclear Medicine 2005,46(6).
9. Germano G, Kavanagh PB, Su HT, Mazzanti M, Kiat H, Hachamovitch R et al. Automatic reorientation of three-dimensional, transaxial myocardial perfusion SPECT images. J Nuclear Medicine: Official Publication Soc Nuclear Med 1995,36(6).
10. Hoffman EJ, Huang SC, Phelps ME. Quantitation in positron emission computed tomography: 1. Effect of object size. J Comput Assist tomography 1979,3(3).
11. Lin GS, Hines HH, Grant G, Taylor K, Ryals C. Automated quantification of defects and wall motion defects by use of cardiac SPECT polar mapping and 4-dimensional surface rendering. J Nucl Med Technol 2006,34(1).
12. Cauvin JC, Boire JY, Maublant JC, Bonny JM, Zanca M, Veyre A. Automatic detection of the left ventricular myocardium long axis and center in thallium-201 single photon emission computed tomography. Eur J Nucl Med 1992,19(12).
13. Mullick R, Ezquerra NF. Automatic determination of LV orientation from SPECT data. IEEE Trans Med Imaging 1995,14(1).
14. deKemp RA, Nahmias C. Automated determination of the left ventricular long axis in cardiac positron tomography. Physiol Meas 1996,17(2).
15. Karimi-Ashtiani S, Arsanjani R, Fish M, Kavanagh P, Germano G, Berman D et al. Direct quantification of left ventricular motion and thickening changes using rest-stress myocardial perfusion SPECT. Journal of nuclear medicine: official publication. Soc Nuclear Med 2012,53(9).
16. Faber TL, Cooke CD, Folks RD, Vansant JP, Nichols KJ, DePuey EG et al. Left ventricular function and perfusion from gated SPECT perfusion images: an integrated method. J Nuclear Medicine: Official Publication Soc Nuclear Med 1999,40(4).
17. Germano G, Erel J, Lewin H, Kavanagh PB, Berman DS. Automatic quantitation of Regional Myocardial Wall Motion and Thickening from Gated Technetium-99m Sestamibi Myocardial Perfusion single-Photon Emission Computed Tomography. J Am Coll Cardiol 1997,30(5).
18. Germano G, Kavanagh PB, Kavanagh JT, Wishner SH, Berman DS, Kavanagh GJ. Repeatability of automatic left ventricular cavity volume measurements from myocardial perfusion SPECT. J Nuclear Cardiol 1998,5(5).
19. Cooke CD, Vansant JP, Krawczynska EG, Faber TL, Garcia EV. Clinical validation of three-dimensional color-modulated displays of myocardial perfusion. J Nuclear Cardiol 1997,4(2P1).

20. Faber TL, Cooke CD, Folks RD, Vansant JP, Nichols J, DePuey EG et al. Left ventricular function and perfusion from gated SPECT perfusion images: an integrated method. J Nuclear Medicine: Official Publication Soc Nuclear Med 1999,40(4).
21. Zhang D, Pretorius PH, Lin K, Miao W, Li J, King MA et al. A novel deep-learning–based approach for automatic reorientation of 3D cardiac SPECT images. Eur J Nucl Med Mol Imaging 2021,48(11).
22. Moudi M, Al, Sun Z, Lenzo N. Diagnostic value of SPECT, PET and PET/CT in the diagnosis of coronary artery disease: a systematic review. Biomed Imaging Interv J 2011,7(2).
23. Rahmim A, Zaidi H. PET versus SPECT: strengths, limitations and challenges. Nucl Med Commun 2008,29(3).
24. Rischpler C, Nekolla S, Schwaiger M. PET and SPECT in heart failure. Curr Cardiol Rep 2013,15(3).
25. Hage FG, AlJaroudi WA. Review of cardiovascular imaging in the Journal of Nuclear Cardiology in 2017. Part 2 of 2: myocardial perfusion imaging. J Nuclear Cardiology: Official Publication Am Soc Nuclear Cardiol 2018,25(4).
26. Su TY, Chen JJ, Chen WS, Chang YH, Lu HHS. Deep learning for defects auxiliary diagnosis using CZT SPECT myocardial perfusion imaging. J Chin Med Association 2023,86(1).
27. Daniel EB. Watershed modeling and its applications: a state-of-the-art review. Open Hydrology J 2011,5(1).
28. Perez A, Gonzalez RC. An iterative thresholding algorithm for image segmentation. IEEE Trans Pattern Anal Mach intelligence 1987,9(6).
29. Drever L, Roa W, McEwan A, Robinson D. Iterative threshold segmentation for PET target volume delineation. Med Phys 2007,34(4).
30. Li D, Li W, Liao Q. Active contours driven by local and global probability distributions. J Vis Commun Image Represent 2013,24(5).
31. Ding K, Xiao L, Weng G. Active contours driven by local pre-fitting energy for fast image segmentation. Pattern Recognit Lett 2018,104(104).
32. Pang J, Miller E, Jeffrey D, Tassinari A, McAlindon T. A curve evolution method for identifying weak edges with applications to the segmentation of magnetic resonance images of the knee. 2011 IEEE International Symposium on Biomedical Imaging 2011:1410–1415.
33. Haralick RM, Shapiro LG. Image segmentation techniques. Computer vision. Graphics Image Process 1985,29(1).
34. Nikhil RP, Sankar KP. A review on image segmentation techniques. Pattern Recogn 1993,26(9).
35. Blackwell D, MacQueen JB. Ferguson distributions via Pólya urn schemes. Ann Stat. 1973;1:353–5.
36. Vovk U, Pernus F, Likar B. A review of methods for correction of intensity inhomogeneity in MRI. IEEE Trans Med Imaging 2007,26(3).
37. Li C, Gore JC, Davatzikos C. Multiplicative intrinsic component optimization (MICO) for MRI bias field estimation and tissue segmentation. Magn Reson Imaging 2014,32(7).
38. Ji Z, Xia Y, Sun Q, Cao G, Chen Q. Active contours driven by local likelihood image fitting energy for image segmentation. Inf Sci 2015,301(301).
39. Ding K, Xiao L, Weng G. Active contours driven by region-scalable fitting and optimized Laplacian of Gaussian energy for image segmentation. Sig Process 2017,134(134).
40. Li H, He H, Wen Y. Dynamic particle swarm optimization and K-means clustering algorithm for image segmentation. Optik - Int J Light Electron Opt 2015,126(24).
41. Salmeron JL, Rahimi SA, Navali AM, Sadeghpour A. Medical diagnosis of rheumatoid arthritis using data driven PSO–FCM with scarce datasets. Neurocomputing 2016,232(232).
42. Garcia EV, Cooke CD, Van KF, Folks R, Peifer J, DePuey E et al. Technical aspects of myocardial spect imaging with technetium-99m sestamibi. Am J Cardiol 1990,66(13).
43. Klein R, Beanlands RSB, deKemp RA. Quantification of myocardial blood flow and flow reserve: technical aspects. J Nuclear Cardiology: Official Publication Am Soc Nuclear Cardiol 2010,17(4).
44. Eckstein J, Bertsekas DP. On the Douglas—Rachford splitting method and the proximal point algorithm for maximal monotone operators. Math Program. 1992;55:1–3.
45. Cerqueira MD, Weissman NJ, Dilsizian V, Jacobs AK, Kaul S, Laskey WK et al. Standardized myocardial segmentation and nomenclature for tomographic imaging of the heart. A statement for healthcare professionals from the Cardiac Imaging Committee of the Council on Clinical Cardiology of the American Heart Association. Circulation 2002,105(4).
46. Zhu F, Li L, Zhao J, Zhao C, Tang S, Nan J et al. A new method incorporating deep learning with shape priors for left ventricular segmentation in myocardial perfusion SPECT images. Comput Biol Med 2023,160():106954.
47. Nekolla SG, Miethaner C, Nguyen N, Ziegler SI, Schwaiger M. Reproducibility of polar map generation and assessment of defect severity and extent assessment in myocardial perfusion imaging using positron emission tomography. Eur J Nucl Med 1998,25(9).